The color gradients of the globular cluster systems in M87 and M49

Wu, Yiming; Liu, Chengze; Peng, Eric W.; Ko, Youkyung; Côté, Patrick; Jain, Rashi; Ferrarese, Laura; Yang, Xiaohu; Lançon, Ariane; Puzia, Thomas; Lim, Sungsoon

Publisher's version / Version de l'éditeur:
https://doi.org/10.3847/1538-4357/ac45fe
The Astrophysical Journal, 926, 2, p. 149, 2022-02-01

The Astrophysical Journal, 926:149 (7pp), 2022 February 20 https://doi.org/10.3847/1538-4357/ac45fe

The Color Gradients of the Globular Cluster Systems in M87 and M49

Yiming Wu[1], Chengze Liu[1], Eric W. Peng[2,3], Youkyung Ko[4], Patrick Côté[5], Rashi Jain[6], Laura Ferrarese[5], Xiaohu Yang[1], Ariane Lançon[6], Thomas Puzia[7], and Sungsoon Lim[8]
[1] Department of Astronomy, School of Physics and Astronomy, and Shanghai Key Laboratory for Particle Physics and Cosmology, Shanghai Jiao Tong University, Shanghai 200240, People's Republic of China; czliu@sjtu.edu.cn
[2] Department of Astronomy, Peking University, Beijing 100871, People's Republic of China
[3] Kavli Institute for Astronomy and Astrophysics, Peking University, Beijing 100871, People's Republic of China
[4] Korea Astronomy and Space Science Institute, 776 Daedeok-daero, Yuseong-Gu, Daejeon 34055, Korea
[5] Herzberg Astronomy and Astrophysics Research Centre, National Research Council of Canada, 5071 W. Saanich Road, Victoria, BC, V9E 2E7, Canada
[6] Université de Strasbourg, CNRS, Observatoire astronomique de Strasbourg, UMR7550, F-67000, Strasbourg, France
[7] Instituto de Astrofísica, Pontificia Universidad Católica de Chile, Av. Vicuña Mackenna 4860, 7820436 Macul, Santiago, Chile
[8] Department of Astronomy, Yonsei University, 50 Yonsei-ro Seodaemun-gu, Seoul 03722, Korea
Received 2021 July 27; revised 2021 November 11; accepted 2021 December 21; published 2022 February 21

Abstract

Combining data from the ACS Virgo Cluster Survey and the Next Generation Virgo cluster Survey, we extend previous studies of color gradients of the globular cluster (GC) systems of the two most massive galaxies in the Virgo cluster, M87 and M49, to radii of $\sim 15\,R_e$ ($\sim$200 kpc for M87 and $\sim$250 kpc for M49, where R_e is the effective radius). We find significant negative color gradients, i.e., becoming bluer with increasing distance, out to these large radii. The gradients are driven mainly by the outward decrease in the ratio of red to blue GC numbers. The color gradients are also detected out to $\sim 15\,R_e$ in the red and blue subpopulations of GCs taken separately. In addition, we find a negative color gradient when we consider the satellite low-mass elliptical galaxies as a system, i.e., the satellite galaxies closer to the center of the host galaxy usually have redder color indices, for both their stars and their GCs. According to the "two phase" formation scenario of massive early-type galaxies, the host galaxy accretes stars and GCs from low-mass satellite galaxies in the second phase. So an accreted GC system naturally inherits the negative color gradient present in the satellite population. This can explain why the color gradient of the GC system can still be observed at large radii after multiple minor mergers.

Unified Astronomy Thesaurus concepts: Globular star clusters (656); Galaxy evolution (594); Early-type galaxies (429); Giant elliptical galaxies (651)

1. Introduction

Most, but not all, galaxies show negative color gradients, i.e., the stellar components are redder in the core region of the galaxy than in its outskirts (e.g., Liu et al. 2009; Roediger et al. 2011b; Loubser & Sánchez-Blázquez 2012; Kennedy et al. 2016; Zheng et al. 2017; Liang & Li 2018; Suess et al. 2019; Domínguez Sánchez et al. 2020). The color gradients of most early-type galaxies (ETGs) are mainly due to the radial variation of metallicity, while the origin of color gradients in late-type galaxies is much more complicated (e.g., Liu et al. 2005; Roediger et al. 2011a, 2012; Mihos et al. 2013; Goddard et al. 2017; Peterken et al. 2020). The steepness and sign of color gradients are closely related to the formation and assembly history of galaxies, e.g., the monolithic collapse formation scenario predicts the existence of negative color gradients (e.g., Naab et al. 2009; Pipino et al. 2010; Nelson et al. 2016; Taylor & Kobayashi 2017) while galaxy assembly through mergers (either major or minor) tends to flatten existing gradients (e.g., Kobayashi 2004; Di Matteo et al. 2009; Tortora & Napolitano 2012; Oyarzún et al. 2019).

According to the standard cosmological model, massive galaxies are believed to form hierarchically. In this framework, the formation of massive ETGs has been well described by a "two phase" formation scenario (e.g., Côté et al. 1998; Oser et al. 2010; Johansson et al. 2012; Huang et al. 2013; Modak et al. 2017; Dolfi et al. 2021). In this scenario, the stars formed in situ though the dissipative collapse of gas at an early stage, and this was followed by a second phase of successive minor mergers, which accrete stars (formed ex situ) from smaller satellite galaxies. The fraction of ex situ stars increases with radius and dominates in the outskirts of the galaxy (Davison et al. 2021; Pulsoni et al. 2021). These accreted stars increase the masses and sizes of the main galaxies (e.g., Naab et al. 2009; Oser et al. 2012; Karademir et al. 2019) and modify the color (stellar population) profiles, especially in the galaxies' outskirts (e.g., Di Matteo et al. 2009; Guo et al. 2011; Tortora & Napolitano 2012; Zibetti et al. 2020). Karademir et al. (2019) investigated how the orbit configurations influence the mass distribution of the merger remnant and the disrupted satellite galaxy. They found that the streams are usually the result of nearly circular infall while the shell structures are made from radial satellite infall. Different merger events modify the mass and stellar population distribution in different ways. The Feedback in Realistic Environments (FIRE) and FIRE-2 simulations (Hopkins et al. 2014, 2018) investigated how the feedbacks influence the mass growth, the morphology, the quenching, and other properties of galaxies. In particular, they showed that the feedback from rapid infall and strong outflow can stir the distribution of gas and stars, and flatten the metallicity gradient (Ma et al. 2016, 2017).

The investigation of color/metallicity profiles and their gradients, especially at large radii, can give hints of the formation and assembly history of massive ETGs. However, the low surface brightness of galaxies' outskirts makes it difficult to study their profiles at very large radii, even when

stacking high-quality deep images (Huang et al. 2018, and references therein).

As some of the oldest stellar systems in the universe, globular clusters (GCs) are tightly tied to the formation and assembly history of their host galaxies. In addition, GCs are much easier to observe than individual stars since they are compact and much brighter (e.g., Harris 2009a; Forbes et al. 2011; Pastorello et al. 2015; Forte et al. 2019). So the GC system is an alternative and unique probe of the formation and assembly history of its host galaxy.

Using GC systems as probes, Côté et al. (1998) investigated the formation and evolution of massive ETGs. They originally proposed that the red (metal-rich) GCs are the intrinsic population and the blue (metal-poor) GCs are accreted from other galaxies, and the number ratio of blue and red GCs can estimate the merger history of the massive ETG. Simulation studies predicted that the blue GCs formed at an early time ($z \sim 4$) in low-mass halos while the red GCs formed later ($z \sim 2$) in more massive halos (Choksi et al. 2018; El-Badry et al. 2019; Reina-Campos et al. 2019). With the hierarchical growth, massive galaxies will naturally have red and blue GC populations.

Based on data from the Advanced Camera for Surveys (ACS) Virgo Cluster Survey (ACSVCS, Côté et al. 2004) and the ACS Fornax Cluster Survey (ACSFCS, Jordán et al. 2007a), Liu et al. (2011) studied the color and metallicity gradients of GC systems of Virgo and Fornax ETGs. They found that the GC systems in most ETGs have negative color/metallicity gradients, which is consistent with the results of other studies (e.g., Harris 2009a, 2009b; Faifer et al. 2011; Pastorello et al. 2015; Ko et al. 2019). However, the field of view of the Hubble Space Telescope/ACS is relatively small, being $202'' \times 202''$, and can only cover approximately the effective radius R_e for the most massive ETGs in the Virgo cluster.

The Next Generation Virgo Cluster Survey (NGVS, Ferrarese et al. 2012) is a deep, multiwavelength imaging survey that covers the whole Virgo cluster ($\sim$104 deg^2). Based on the excellent NGVS images, several papers have been published to investigate the GCs in the Virgo cluster (Durrell et al. 2014; Muñoz et al. 2014; Zhu et al. 2014; Zhang et al. 2015, 2018; Powalka et al. 2016a, 2016b, 2017, 2018; Toloba et al. 2016; Longobardi et al. 2018; Sun et al. 2019; Taylor et al. 2021). With the combination of ACSVCS (high spatial resolution) and NGVS (wide field of view) data, we have a unique chance to study the color gradients of GC systems of massive ETGs over a very large range in radius (from the center to the edge of the galaxy).

In this study, we will focus on the two most massive ETGs in the Virgo cluster, M87 (VCC 1316) and M49 (VCC 1226), which have likely undergone many major/minor mergers in their assembly history. We will introduce the data and GC sample selection in Section 2. In Section 3, we present our results and the discussion, and in Section 4 we give a brief summary of our findings. We adopt an effective radius $R_e = 171.''71 \simeq 13.74$ kpc for M87 and $R_e = 209.''15 \simeq 16.73$ kpc for M49 (Ferrarese et al. 2006) in this study.

2. Data and GC Sample

To study the GC systems over a large range in radius, we combine the data from ACSVCS (central region) and NGVS (surrounding area). The details of GC selection in ACSVCS have been well described in Peng et al. (2006) and Jordán et al. (2009). For NGVS data, Muñoz et al. (2014) have described GC selection using the uiK_s color–color diagram. By adding minimal information on the morphology of GCs to the colors, one significantly reduces contamination by foreground stars and background galaxies (Liu et al. 2015, 2020; Powalka et al. 2016a; González-Lópezlira et al. 2017; Voggel et al. 2020). In the present study, all the results are based on samples obtained with methods that exploit colors and at least one morphological criterion jointly. For the M87 region, E. W. Peng et al. (2022, in preparation) extended the sample of Powalka et al. (2016a) to fainter GC candidates; for the M49 region, R. Jain et al. (2022, in preparation) exploited new near-IR data to produce a sample of GC candidates with similar criteria.

As discussed in Muñoz et al. (2014), the selected GC sample is very clean when the uncertainty of magnitude is smaller than 0.05 mag, which corresponds to $g \sim 24$ mag for NGVS data. In this study, to make the combined GC sample as homogeneous as possible, we adopt an additional magnitude cut of $g < 23.9$ mag for both ACSVCS and NGVS GCs, which is the turnover magnitude of the GC luminosity function in ETGs (Jordán et al. 2007b; Villegas et al. 2010). In fact, the depth of K_s-band data affects our GC selection. At constant g-band magnitude, bluer GCs are always fainter in the K_s-band. So there will be a bias toward selecting slightly redder GCs. We measure the color gradients using a GC sample selected based on optical data only (no bias) and a GC sample selected based on optical and K_s-band data. The difference between the two measurements is quite small. That means the selection bias happens at all radii, so may not affect the gradient measurements.

According to previous studies (Durrell et al. 2014; Oldham & Auger 2016; Ko et al. 2017), the GC number density profile changes slope at $\sim$50′–60′ for M87, and $\sim$45′–60′ for M49, which corresponds to $\sim$15 R_e for these two galaxies. So, we measure the color gradients of GC systems in the range from 0.1 to 15 R_e to remove the effect at the galaxy center and that of intracluster GCs. The GCs around satellite galaxies and bright stars are also eliminated from the final sample.

The ACSVCS imaging was taken in two filters: F475W ($\approx$SDSS g) and F850LP ($\approx$SDSS z), which are slightly different from the CFHT/Megacam g- and z-bands used for the NGVS. We use M87 and M49 GC candidates that appear in both ACSVCS and NGVS samples to calculate the transformation between ACSVCS ($g_{\rm ACSVCS}$, $z_{\rm ACSVCS}$) and NGVS ($g_{\rm NGVS}$, $z_{\rm NGVS}$) magnitudes, as shown in Figure 1. The following equations are adopted to transform the magnitudes between ACSVCS and NGVS:

$$\begin{aligned} g_{\rm NGVS} &= g_{\rm ACSVCS} - 0.013 - 0.082 \times (g - z)_{\rm ACSVCS} \\ z_{\rm NGVS} &= z_{\rm ACSVCS} - 0.023 + 0.027 \times (g - z)_{\rm ACSVCS}. \end{aligned} \quad (1)$$

Following Liu et al. (2011), the radial color gradient is defined as

$$G_{g-z} = \frac{\Delta(g - z)_0}{\Delta \log R}, \quad (2)$$

where $(g - z)_0$ is the color index corrected for Galactic extinction and R is the projected distance from the galaxy center.

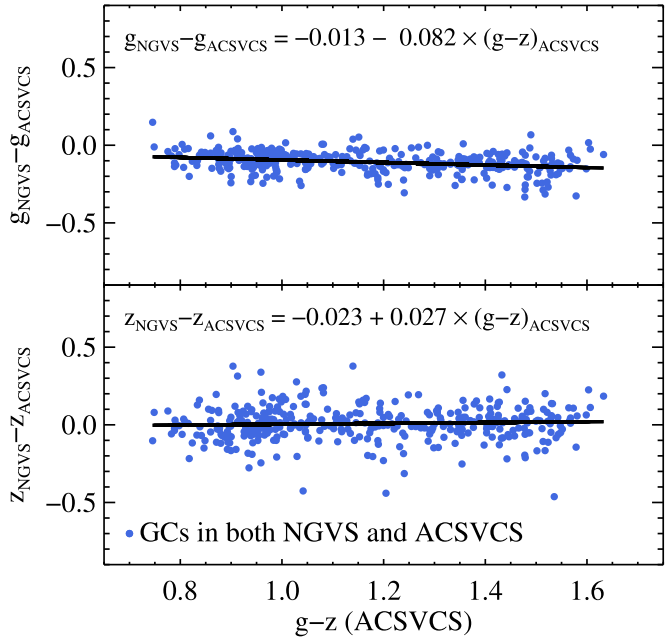

Figure 1. The transformation between ACSVCS and NGVS for the g band (upper panel) and z band (lower panel). The blue dots are GC candidates that were detected in both ACSVCS and NGVS around M87 and M49. The black line in each panel shows the best linear fit for the blue dots. The transformation equations adopted in this study are shown at the top of the panels.

3. Results and Discussion

3.1. The Gradients of GC Systems

Figures 2(a), (c), and (e) show the spatial distribution, $(g-z)_0$, and [Fe/H] profiles for ACSVCS GCs (green dots) that are in the central region ($\lesssim 1\ R_e$) of M87, respectively. Meanwhile, Figures 2(b), (d), and (g) show the plots for ACSVCS GCs (green dots) and NGVS GCs (blue dots) that cover a much larger region ($<15\ R_e$). We measure the mean values of $(g-z)_0$ and [Fe/H] in different radius bins and show these as the black filled circles in the lower four panels. The color gradient of GC systems in the central region (ACSVCS GCs only, panel (c)) is -0.110 ± 0.034, which means that the GCs are bluer as one goes outward. However, the color gradient for the whole GC system (ACSVCS+NGVS GCs, panel (d)) is much steeper (-0.174 ± 0.004). As can be seen in Figure 2(d), the numbers of red and blue GCs are comparable in the central region (see also Peng et al. 2006) but GCs are dominated by the blue subpopulation at larger radii. Such a distribution of red and blue GCs will cause a steeper color gradient for the whole GC system (e.g., Harris et al. 2006; Wehner et al. 2008; Caso et al. 2017; Forbes & Remus 2018; Ko et al. 2019; De Bórtoli et al. 2020; Taylor et al. 2021).

Besides the color gradients, we convert the color index to metallicity [Fe/H] according to the nonlinear color–metallicity relation in Blakeslee et al. (2010) and calculate the metallicity gradient ($G_{[Fe/H]} \equiv \Delta[Fe/H]/\Delta \log R$) of the GC system. We show the [Fe/H] profiles for GC systems of M87 in Figures 2(e) and 2(f). The [Fe/H] gradient in the central region is -0.482 ± 0.140 and the gradient for the whole GC system is -0.992 ± 0.027. It is noteworthy that both the color and metallicity gradients are flatter in the central region of M87 than further out.

We also investigate the GC system of another massive galaxy, M49, which is the most massive galaxy in the Virgo cluster and the central galaxy of subcluster B (Boselli et al. 2014). The results are shown in Figure 3. The color and [Fe/H] gradients are -0.094 ± 0.062 and -0.387 ± 0.234 in the central region while they are -0.157 ± 0.007 and -0.810 ± 0.041 for the whole GC systems. Again, the gradients in the central region are quite flat but the gradients for the whole GC systems are much more significant and steeper.

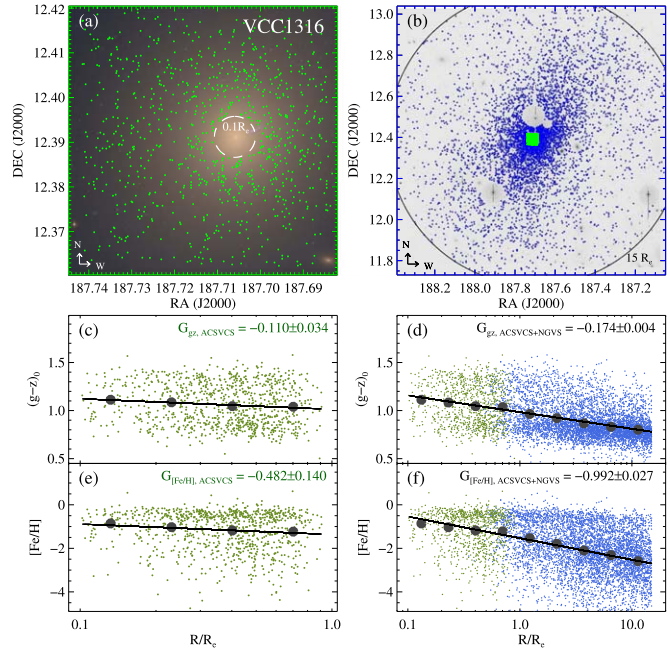

Figure 2. (a) The central region of M87 (VCC 1316) and the spatial distribution of ACSVCS GCs (green dots). The dashed circle has radius 0.1 R_e. (b) The spatial distribution of ACSVCS GCs (green dots) and NGVS GCs (blue dots). The black solid circle has radius 15 R_e. (c) Color profile of ACSVCS GCs. (d) Color profile of ACSVCS GCs (green dots) and NGVS GCs (blue dots). (e) Metallicity profile of ACSVCS GCs. (f) Metallicity profile of ACSVCS GCs (green dots) and NGVS GCs (blue dots). The black filled circles in the lower four panels are the mean values of $(g-z)_0$ or [Fe/H] in given bins and the black lines are the best-fit values for all the data points.

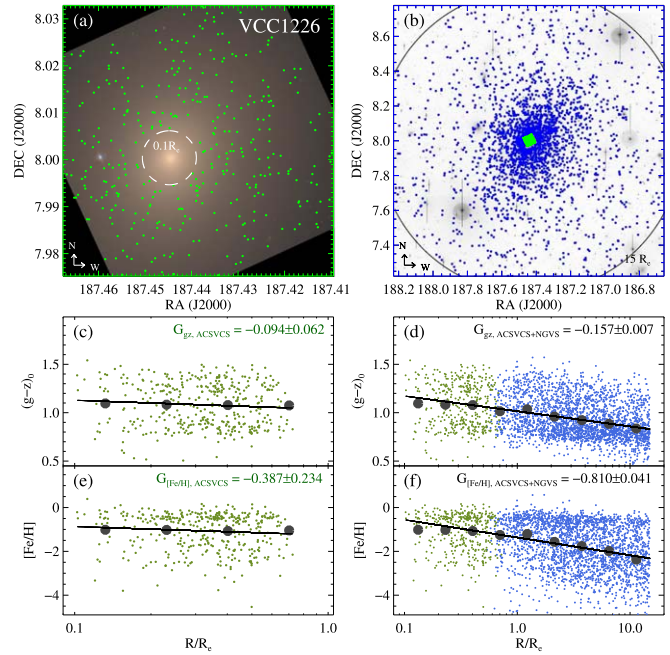

Figure 3. The same as Figure 2, but for M49 (VCC 1226).

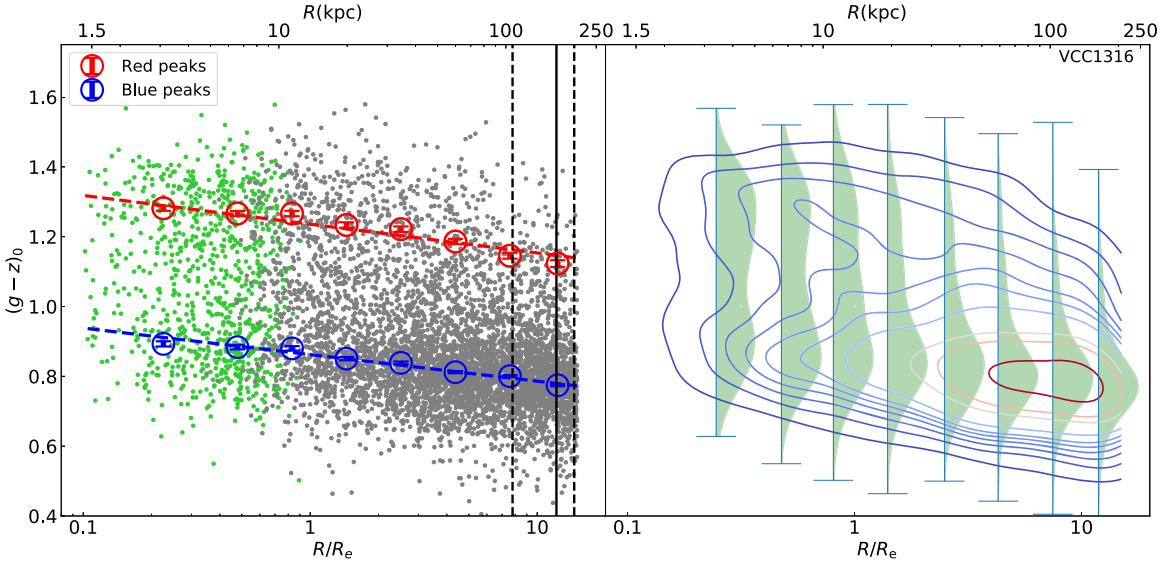

Figure 4. The $(g-z)_0$ color profile for the M87 GC system. Left: the data points, including ACSVCS GCs (green dots) and NGVS GCs (gray dots). The black vertical lines mark the transition radius (solid line) and the errors (dashed lines) found in Ko et al. (2022). Right: map of GC number density overlaid by color distributions in different bins. The red and blue open circles in the left panel represent the peaks of color distributions of subpopulations. The red and blue dashed lines are the corresponding linear fits.

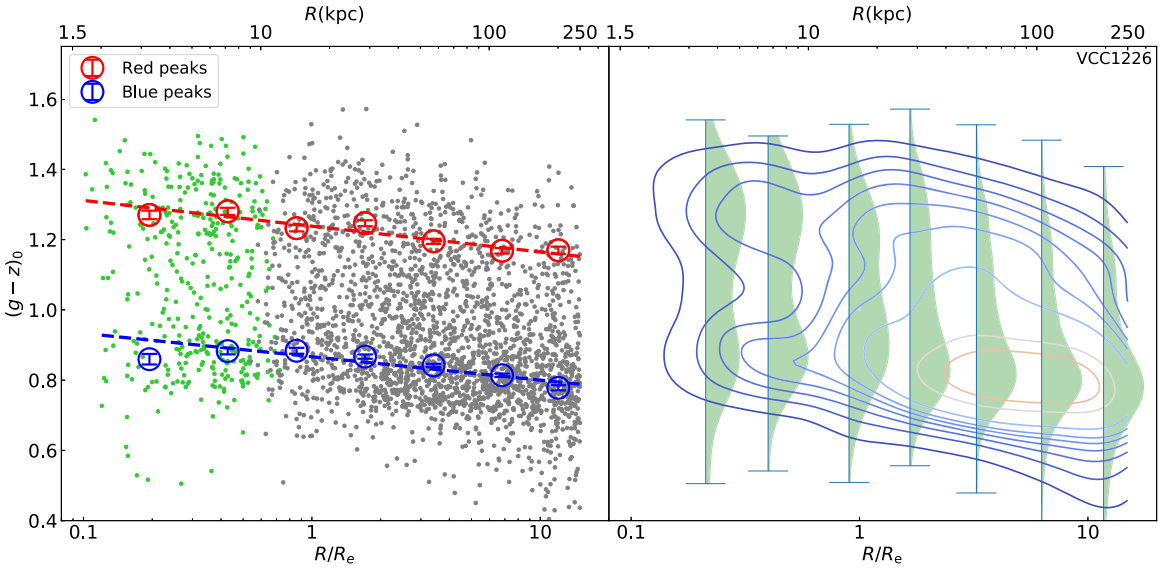

Figure 5. The same as Figure 4, but for the M49 GC system.

3.2. The Color Gradients of GC Subpopulations

One of the most remarkable properties of GC systems in massive galaxies is their bimodal color distribution, with red and blue subpopulations (e.g., Brodie & Strader 2006; Peng et al. 2006; Chies-Santos et al. 2012; Harris et al. 2017; De Bórtoli et al. 2020). It has been widely shown that both red and blue GC subpopulations have negative color/metallicity gradients (e.g., Harris 2009a; Faifer et al. 2011; Liu et al. 2011, 2015; Forte et al. 2012; Kartha et al. 2014; Pastorello et al. 2015; Forbes & Remus 2018). In such cases, it is expected that the "dip" in the color distribution between red and blue peaks will change with galactocentric distance.

Since there are plenty of GCs around M87 and M49, we divide them into several bins according to their galactocentric radii at first, and then we use Kaye's Mixture Model (KMM, McLachlan & Basford 1988; Ashman et al. 1994) to divide the GCs in each radius bin into two subpopulations in the homoscedastic mode, as shown in Figure 4 (GC system of M87) and Figure 5 (GC system of M49). The red and blue open circles in the figures represent the peaks of the color distributions for red and blue subpopulations respectively. The colors of both red and blue subpopulations decline with galactocentric radius continually. The typical colors in different radius bins are almost in a straight line for either the red or blue subpopulation. So we adopt linear fits to the data points and calculate the color gradients for the two subpopulations. The color gradients are $G_{\rm red} = -0.082 \pm 0.005$ and $G_{\rm blue} = -0.076 \pm 0.003$ for the M87 GC system, and $G_{\rm red} = -0.073 \pm 0.007$ and $G_{\rm blue} = -0.067 \pm 0.005$ for the M49 GC system. All the gradients are negative and significant. The gradients of blue and red GCs in these two massive ETGs are comparable, which is consistent with previous studies (Harris 2009b; Liu et al. 2011; Forbes & Remus 2018).

Many studies found a transition in the color/metallicity profile at several effective radii, beyond which the profiles start to flatten, i.e., there are no longer any color gradients (e.g., Harris 2009a; Faifer et al. 2011; Forbes et al. 2011; Strader et al. 2011; Forbes & Remus 2018; Taylor et al. 2021, Ko et al. 2022). However, we do not find such a transition radius in M87 and M49. The color peaks of red and blue subpopulations continue to decline up to $\sim$15 R_e ($\sim$200 kpc for M87 and $\sim$250 kpc for M49). There are several possible reasons for this discrepancy. One reason is that each galaxy has its own assembly history, which is related to its mass and the environment. The transition radius is not a universal property for all galaxies (Remus & Forbes 2021). Another possibility is the purity of the GC sample. As described in previous studies (e.g., Muñoz et al. 2014; Liu et al. 2015, 2020; Longobardi et al. 2018), the contamination of the GC sample in Virgo is mainly due to passive background galaxies. With the increase in contamination at larger radii, the color profile of the GC system could become flat. The third reason is that the definitions of color gradient are different in different studies. There are mainly two different definitions of color gradient in previous studies: $\Delta\mathrm{CI}/\Delta \log R$ and $\Delta\mathrm{CI}/\Delta R$, where CI is the color index and R is the galactocentric radius. As shown in Figures 4 and 5, the color profile is almost a straight line in the CI–$\log R$ diagram. This is the main reason why we define the color gradient as $G = \Delta\mathrm{CI}/\Delta \log R$ in this study. If we show the color profile in the CI–R diagram, the straight line will become a curve, with a steeper slope in the inner region and a shallower slope in the outer region, which seems like a transition.

Ko et al. (2022) investigate the metallicity gradients for spectroscopically confirmed GCs ($g \lesssim 21.5$ mag) around M87 over a very large range of radius (8–837 kpc) and find a transition radius at 169^{+33}_{-60} kpc, beyond which the metallicity gradient of blue GCs turns flat. We show their transition radius (vertical solid line) and the errors (two vertical dashed lines) in the left panel of Figure 4. We can see that the transition radius is close to the boundary of our GC sample. Due to the limitation of our photometric GC sample in this study, we do not rule out the existence of a transition radius.

3.3. The Color Gradients of Satellite Galaxies

According to the "two phase" galaxy formation scenario, massive ETGs accrete stars from smaller satellite galaxies in the second phase. In this process, GCs (usually blue) in satellite galaxies are also accreted by the host galaxy. This is one of the formation scenarios of the blue GC subpopulation in massive ETGs (e.g., Côté et al. 1998; Brodie & Strader 2006; Harris et al. 2017; Kang & Lee 2021). Such a formation scenario raises a question. Why do these accreted GCs have a negative color gradient?

Liu et al. (2016) investigated the [α/Fe] abundance ratio of 11 low-mass ETGs with a large range of clustercentric distances in the Virgo cluster. They found that the galaxies closer to M87 (cluster center) tend to have higher [α/Fe]. Their results imply that the environment is the key factor for the formation of stars and GCs in low-mass ETGs in the galaxy cluster. We select 31 satellite ETGs around M87 ($<15\,R_e$) and 10 satellite ETGs around M49 ($<15\,R_e$) based on the latest NGVS galaxy catalog (Ferrarese et al. 2020). We do not adopt a stellar mass criterion, but all the selected galaxies are certain members of the Virgo cluster, i.e., `class=1` in Table 4 in Ferrarese et al. (2020).

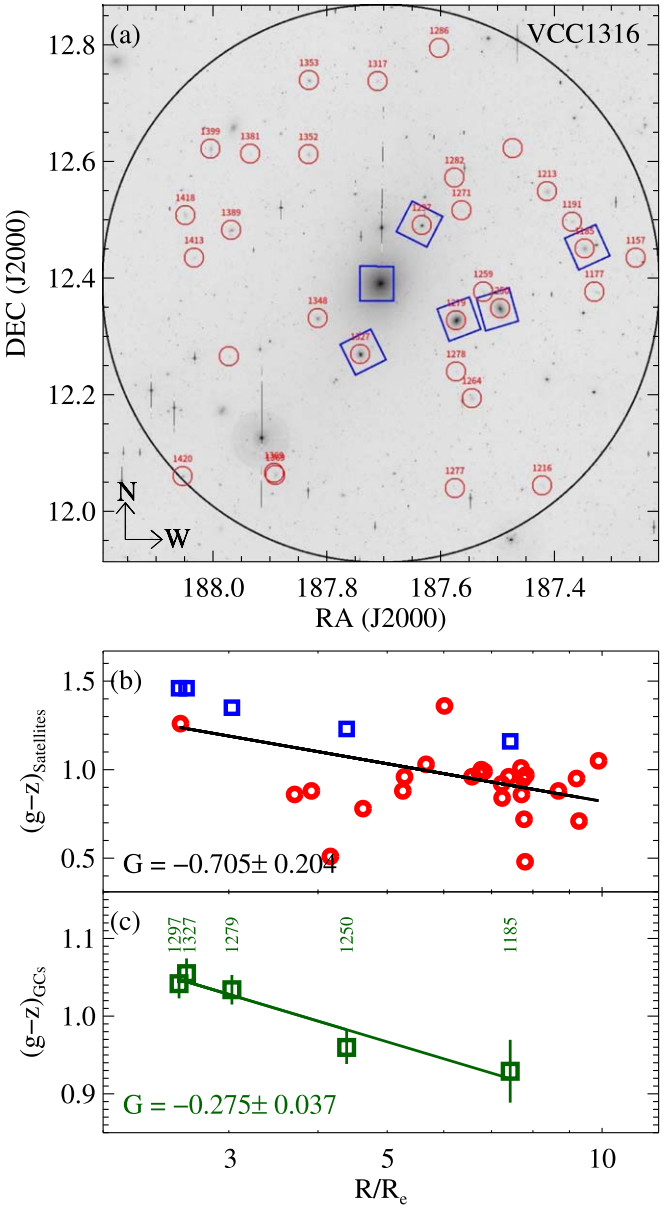

Figure 6. (a) The distribution of satellite ETGs around M87. The ACSVCS galaxies are given by blue squares. The large black circle denotes 15 R_e from M87. (b) The $(g-z)$ color of satellite ETGs as a function of galactocentric radius. (c) The mean colors of GC systems in satellite galaxies as a function of galactocentric radius.

Figure 6(a) shows the spatial distribution and Figure 6(b) the color profile of 31 satellite ETGs around M87. Similar to the result of Liu et al. (2016), the galaxies closer to M87 tend to be redder. Peng et al. (2006) found a positive correlation between the median colors of GC systems and the colors of their host galaxies (see Figure 8 in their paper), i.e., the GCs are usually redder in redder host galaxies. We calculate the mean colors of GC systems in five ACSVCS galaxies and show them as a function of galactocentric radius in Figure 6(c). As expected, the mean colors of GC systems in satellite galaxies decline with galactocentric distance. Figure 7 shows 10 satellite ETGs around M49, including five ACSVCS galaxies. The results for M49 satellite ETGs are the same as for M87 satellite ETGs.

For massive ETGs like M87 and M49, the central regions are dominated by the in situ stars/GCs from a compact progenitor, which are formed at higher redshift and thus with redder colors,

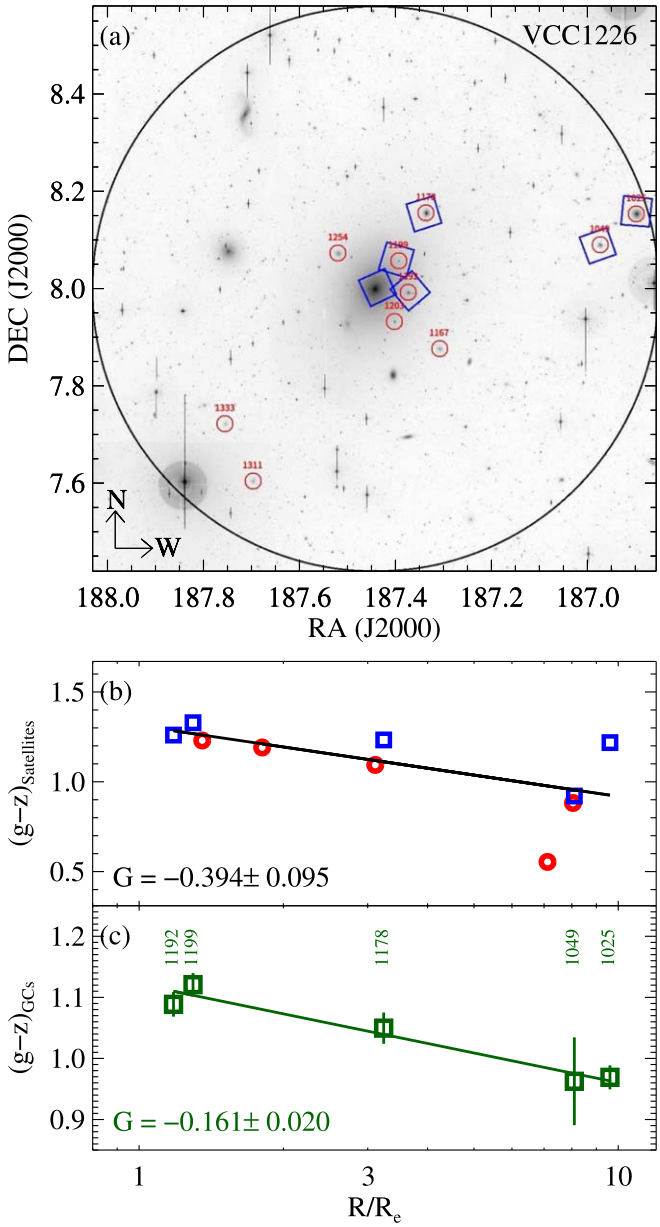

Figure 7. The same as Figure 6, but for satellite galaxies around M49.

and the outer regions are dominated by the ex situ stars/GCs accreted by the satellite galaxies (e.g., Karademir et al. 2019; Pulsoni et al. 2021). The existence of a color gradient in the satellite galaxy system can explain the color gradients of the GC system around massive ETGs in the framework of the "two phase" galaxy formation scenario. Early-stage major mergers mainly influence the distribution of GCs in the central region and flatten pre-existing gradients (Di Matteo et al. 2009; Tortora & Napolitano 2012; Oyarzún et al. 2019), while the following successive minor mergers in the second phase provide GCs to the outer regions. As implied in Figures 6(c) and 7(c), the GCs accreted from these satellite galaxies naturally have a negative color gradient.

4. Summary

With the combination of GC samples from ACSVCS and NGVS, we mainly investigate the color gradients of GC systems in M87 and M49 over a very large range of radius, from the central region to 15 R_e (∼200 kpc for M87 and ∼250 kpc for M49). We find that:

1. The color and metallicity of the whole GC system continue to decline with galactocentric radius, from 0.1 to 15 R_e. The gradient is shallower in the central region ($\lesssim R_e$).
2. Both the red and blue GC subpopulations show significant negative color gradients over a large range of galactocentric radius (0.1–15 R_e). We do not find any sign of transition in the color profiles.
3. The satellite ETGs closer to the center of the host galaxy tend to be redder, as do their GC systems. In an accretion scenario, this may naturally explain the color gradients seen in the GC systems of massive galaxies.

The authors acknowledge support from the National Natural Science Foundation of China (NSFC, grant Nos. 12173025, 11673017, 11833005, 11933003, 11890692, 11621303). This work is also supported by the Shanghai Natural Science Foundation (grant No. 15ZR1446700), 111 project (No. B20019), Shanghai Key Laboratory for Particle Physics and Cosmology (SKLPPC), and Key Laboratory for Particle Physics, Astrophysics and Cosmology, Ministry of Education. We also acknowledge the science research grants from the China Manned Space Project with NO. CMS-CSST-2021-A02.

Facility: HST, CFHT.

ORCID iDs

Chengze Liu https://orcid.org/0000-0002-4718-3428
Eric W. Peng https://orcid.org/0000-0002-2073-2781
Youkyung Ko https://orcid.org/0000-0001-6333-599X
Patrick Côté https://orcid.org/0000-0003-1184-8114
Laura Ferrarese https://orcid.org/0000-0002-8224-1128
Xiaohu Yang https://orcid.org/0000-0003-3997-4606
Ariane Lançon https://orcid.org/0000-0002-7214-8296
Thomas Puzia https://orcid.org/0000-0003-0350-7061
Sungsoon Lim https://orcid.org/0000-0002-5049-4390

References

Ashman, K. M., Bird, C. M., & Zepf, S. E. 1994, AJ, 108, 2348
Blakeslee, J. P., Cantiello, M., & Peng, E. W. 2010, ApJ, 710, 51
Boselli, A., Voyer, E., Boissier, S., et al. 2014, A&A, 570, A69
Brodie, J. P., & Strader, J. 2006, ARA&A, 44, 193
Caso, J. P., Bassino, L. P., & Gómez, M. 2017, MNRAS, 470, 3227
Chies-Santos, A. L., Larsen, S. S., Cantiello, M., et al. 2012, A&A, 539, A54
Choksi, N., Gnedin, O. Y., & Li, H. 2018, MNRAS, 480, 2343
Côté, P., Blakeslee, J. P., Ferrarese, L., et al. 2004, ApJS, 153, 223
Côté, P., Marzke, R. O., & West, M. J. 1998, ApJ, 501, 554
Davison, T. A., Norris, M. A., Leaman, R., et al. 2021, MNRAS, 507, 3089
De Bórtoli, B. J., Bassino, L. P., Caso, J. P., & Ennis, A. I. 2020, MNRAS, 492, 4313
Di Matteo, P., Pipino, A., Lehnert, M. D., Combes, F., & Semelin, B. 2009, A&A, 499, 427
Dolfi, A., Forbes, D. A., Couch, W. J., et al. 2021, MNRAS, 504, 4923
Domínguez Sánchez, H., Bernardi, M., Nikakhtar, F., Margalef-Bentabol, B., & Sheth, R. K. 2020, MNRAS, 495, 2894
Durrell, P. R., Côté, P., Peng, E. W., et al. 2014, ApJ, 794, 103
El-Badry, K., Quataert, E., Weisz, D. R., Choksi, N., & Boylan-Kolchin, M. 2019, MNRAS, 482, 4528
Faifer, F. R., Forte, J. C., Norris, M. A., et al. 2011, MNRAS, 416, 155
Ferrarese, L., Côté, P., Cuillandre, J.-C., et al. 2012, ApJS, 200, 4
Ferrarese, L., Côté, P., Jordán, A., et al. 2006, ApJS, 164, 334
Ferrarese, L., Côté, P., MacArthur, L. A., et al. 2020, ApJ, 890, 128
Forbes, D. A., & Remus, R.-S. 2018, MNRAS, 479, 4760

Forbes, D. A., Spitler, L. R., Strader, J., et al. 2011, MNRAS, 413, 2943
Forte, J. C., Cellone, S. A., De Rossi, M. E., et al. 2019, MNRAS, 482, 950
Forte, J. C., Vega, E. I., & Faifer, F. 2012, MNRAS, 421, 635
Goddard, D., Thomas, D., Maraston, C., et al. 2017, MNRAS, 466, 4731
González-Lópezlira, R. A., Lomelí-Núñez, L., Álamo-Martínez, K., et al. 2017, ApJ, 835, 184
Guo, Y., Giavalisco, M., Cassata, P., et al. 2011, ApJ, 735, 18
Harris, W. E. 2009a, ApJ, 703, 939
Harris, W. E. 2009b, ApJ, 699, 254
Harris, W. E., Ciccone, S. M., Eadie, G. M., et al. 2017, ApJ, 835, 101
Harris, W. E., Whitmore, B. C., Karakla, D., et al. 2006, ApJ, 636, 90
Hopkins, P. F., Kereš, D., Oñorbe, J., et al. 2014, MNRAS, 445, 581
Hopkins, P. F., Wetzel, A., Kereš, D., et al. 2018, MNRAS, 480, 800
Huang, S., Ho, L. C., Peng, C. Y., Li, Z.-Y., & Barth, A. J. 2013, ApJL, 768, L28
Huang, S., Leauthaud, A., Greene, J. E., et al. 2018, MNRAS, 475, 3348
Johansson, P. H., Naab, T., & Ostriker, J. P. 2012, ApJ, 754, 115
Jordán, A., Blakeslee, J. P., Côté, P., et al. 2007a, ApJS, 169, 213
Jordán, A., McLaughlin, D. E., Côté, P., et al. 2007b, ApJS, 171, 101
Jordán, A., Peng, E. W., Blakeslee, J. P., et al. 2009, ApJS, 180, 54
Kang, J., & Lee, M. G. 2021, ApJ, 914, 20
Karademir, G. S., Remus, R.-S., Burkert, A., et al. 2019, MNRAS, 487, 318
Kartha, S. S., Forbes, D. A., Spitler, L. R., et al. 2014, MNRAS, 437, 273
Kennedy, R., Bamford, S. P., Häußler, B., et al. 2016, A&A, 593, A84
Ko, Y., Hwang, H. S., Lee, M. G., et al. 2017, ApJ, 835, 212
Ko, Y., Lee, M. G., Park, H. S., et al. 2019, ApJ, 872, 202
Ko, Y., et al. 2022, ApJ, submitted
Kobayashi, C. 2004, MNRAS, 347, 740
Liang, Z.-X., & Li, C. 2018, RAA, 18, 143
Liu, C., Côté, P., Peng, E. W., et al. 2020, ApJS, 250, 17
Liu, C., Peng, E. W., Côté, P., et al. 2015, ApJ, 812, 34
Liu, C., Peng, E. W., Jordán, A., et al. 2011, ApJ, 728, 116
Liu, C., Shen, S., Shao, Z., et al. 2009, RAA, 9, 1119
Liu, Y., Peng, E. W., Blakeslee, J., et al. 2016, ApJ, 818, 179
Liu, Y., Zhou, X., Ma, J., et al. 2005, AJ, 129, 2628
Longobardi, A., Peng, E. W., Côté, P., et al. 2018, ApJ, 864, 36
Loubser, S. I., & Sánchez-Blázquez, P. 2012, MNRAS, 425, 841
Ma, X., Hopkins, P. F., Faucher-Giguère, C.-A., et al. 2016, MNRAS, 456, 2140
Ma, X., Hopkins, P. F., Feldmann, R., et al. 2017, MNRAS, 466, 4780
McLachlan, G. J., & Basford, K. E. 1988, Mixture Models. Inference and Applications to Clustering (New York: Marcel Dekker)
Mihos, J. C., Harding, P., Rudick, C. S., & Feldmeier, J. J. 2013, ApJL, 764, L20
Modak, S., Chattopadhyay, T., & Chattopadhyay, A. K. 2017, Ap&SS, 362, 206
Muñoz, R. P., Puzia, T. H., Lançon, A., et al. 2014, ApJS, 210, 4
Naab, T., Johansson, P. H., & Ostriker, J. P. 2009, ApJL, 699, L178
Nelson, E. J., van Dokkum, P. G., Förster Schreiber, N. M., et al. 2016, ApJ, 828, 27
Oldham, L. J., & Auger, M. W. 2016, MNRAS, 455, 820
Oser, L., Naab, T., Ostriker, J. P., & Johansson, P. H. 2012, ApJ, 744, 63
Oser, L., Ostriker, J. P., Naab, T., Johansson, P. H., & Burkert, A. 2010, ApJ, 725, 2312
Oyarzún, G. A., Bundy, K., Westfall, K. B., et al. 2019, ApJ, 880, 111
Pastorello, N., Forbes, D. A., Usher, C., et al. 2015, MNRAS, 451, 2625
Peng, E. W., Jordán, A., Côté, P., et al. 2006, ApJ, 639, 95
Peterken, T., Merrifield, M., Aragón-Salamanca, A., et al. 2020, MNRAS, 495, 3387
Pipino, A., D'Ercole, A., Chiappini, C., & Matteucci, F. 2010, MNRAS, 407, 1347
Powalka, M., Lançon, A., Puzia, T. H., et al. 2016a, ApJS, 227, 12
Powalka, M., Lançon, A., Puzia, T. H., et al. 2017, ApJ, 844, 104
Powalka, M., Puzia, T. H., Lançon, A., et al. 2016b, ApJL, 829, L5
Powalka, M., Puzia, T. H., Lançon, A., et al. 2018, ApJ, 856, 84
Pulsoni, C., Gerhard, O., Arnaboldi, M., et al. 2021, A&A, 647, A95
Reina-Campos, M., Kruijssen, J. M. D., Pfeffer, J. L., Bastian, N., & Crain, R. A. 2019, MNRAS, 486, 5838
Remus, R.-S., & Forbes, D. A. 2021, arXiv:2101.12216
Roediger, J. C., Courteau, S., MacArthur, L. A., & McDonald, M. 2011a, MNRAS, 416, 1996
Roediger, J. C., Courteau, S., McDonald, M., & MacArthur, L. A. 2011b, MNRAS, 416, 1983
Roediger, J. C., Courteau, S., Sánchez-Blázquez, P., & McDonald, M. 2012, ApJ, 758, 41
Strader, J., Romanowsky, A. J., Brodie, J. P., et al. 2011, ApJS, 197, 33
Suess, K. A., Kriek, M., Price, S. H., & Barro, G. 2019, ApJ, 877, 103
Sun, W., Peng, E. W., Ko, Y., et al. 2019, ApJ, 885, 145
Taylor, M. A., Ko, Y., Côté, P., et al. 2021, ApJ, 915, 83
Taylor, P., & Kobayashi, C. 2017, MNRAS, 471, 3856
Toloba, E., Li, B., Guhathakurta, P., et al. 2016, ApJ, 822, 51
Tortora, C., & Napolitano, N. R. 2012, MNRAS, 421, 2478
Villegas, D., Jordán, A., Peng, E. W., et al. 2010, ApJ, 717, 603
Voggel, K. T., Seth, A. C., Sand, D. J., et al. 2020, ApJ, 899, 140
Wehner, E. M. H., Harris, W. E., Whitmore, B. C., Rothberg, B., & Woodley, K. A. 2008, ApJ, 681, 1233
Zhang, H.-X., Peng, E. W., Côté, P., et al. 2015, ApJ, 802, 30
Zhang, H.-X., Puzia, T. H., Peng, E. W., et al. 2018, ApJ, 858, 37
Zheng, Z., Wang, H., Ge, J., et al. 2017, MNRAS, 465, 4572
Zhu, L., Long, R. J., Mao, S., et al. 2014, ApJ, 792, 59
Zibetti, S., Gallazzi, A. R., Hirschmann, M., et al. 2020, MNRAS, 491, 3562